

P-205L: Late-News Poster: Comparison between a-InGaZnO and a-InHfZnO TFTs in Perspective of Subgap Density of States (DOS) in Active Film

Sangwon Lee, Sungchul Kim, Yong Woo Jeon, Dong Myong Kim, and Dae Hwan Kim^a

School of Electrical Engineering, Kookmin University, Jeongneung-dong, Seongbuk-gu, Seoul 136-702, Republic of Korea.

Je-Hun Lee, Byung Du Ahn, Sei Yong Park, Jun-Hyun Park, Joo Han Kim, and Jaewoo Park

LCD R&D Center, Samsung Electronics, San #24, Nongseo-Dong, Yongin 449-711, Republic of Korea.

Abstract

The extraction of acceptor-like subgap DOS ($g_A(E)$) in a-InGaZnO and a-InHfZnO TFTs is demonstrated by using multi-frequency C-V technique. The DC performance and negative bias stress (NBS)-induced instability are compared in perspective of $g_A(E)$. The superior stability of a-InHfZnO TFT is deduced to be originated from donor-like DOS $g_D(E)$.

1. Introduction

In representative oxide thin film transistors (TFTs), amorphous Indium-Gallium-Zinc-Oxide (a-IGZO) TFTs have attracted much attention as promising candidates substituting a-Si:H and/or low temperature poly-Si (LTPS) TFTs as switching/driving devices in active-matrix liquid crystal display (AMLCD) and active-matrix organic light-emitting diode displays (AMOLED) backplanes [1-4] due to advantages of a high mobility, large area uniform integration, a low cost room temperature fabrication process, and the compatibility with transparent, flexible, and light display applications. Nowadays, the bias stress/temperature/optical illumination-induced instabilities have emerged as critical and urgent issues on ZnO-based TFTs. Paradoxically, it is because that these instabilities cannot be fully understood and controlled in comparison with the ramping up in diverse oxide TFT-based applications.

Various ZnO-based TFTs still exhibit unsolved and complicated bias stress/temperature illumination-induced instabilities [5-6]. Very recently, amorphous Indium-Hafnium-Zinc-Oxide (a-IHZO) TFTs are proposed and developed as the stability-boosted oxide TFTs [7-8]. It is reported that the higher amount of Hf element in the active thin films result in better stability, given their identical device structure, gate insulator, passivation layer, even and fabrication process. It is inferred that the addition of Hf element can suppress the growth of the columnar structure and drastically decrease the carrier concentration and hall mobility in the a-IHZO films. In addition, it is deduced that the Hf ions may play a key role in improving the instability of the TFTs, due to their high oxygen bonding ability [7]. However, the direct comparison between a-IGZO and a-IHZO TFTs in perspective of the quality of active film has been not yet reported.

On the other hand, subgap density of states (DOS) in active film plays a significant role of determining stability as well as performance of ZnO-based TFTs [9]. Since subgap acceptor-like DOS ($g_A(E)$) of *n*-type a-IGZO film is one of most important parameters determining both the electrical characteristic and the

instability, the extraction of $g_A(E)$ in a-IGZO TFTs based on various techniques have been reported by many research groups. Hsieh, Kimura, and co-authors extracted DOS by the numerical simulation-based fitting, where the influence of the free carrier density was assumed to be negligible [10, 11]. Jeon, Park, and co-authors have demonstrated the DOS extraction based on the optical response of capacitance-voltage (C-V) characteristics [12, 13]. However, if the parameter extraction for display applications is adopted to characterize the instabilities of TFTs under real backlight illumination, even though it is a simple and fast extraction method, the DOS extraction technique with additional photons might be a slightly erroneous extraction scheme because the electrical characteristics of TFTs are changed only under optical illumination during photonic C-V characterization. More recently, Chen *et al.* reported a DOS extraction technique based on the Meyer-Neldel rule of the activation energy (E_a) [14]. It is self-consistent method based on the experimentally obtained E_a . However, it is also complicated process in the practical extraction of reliability-related DOS parameters because the temperature-dependence is necessary to be measured.

With these two motivations, in this work, a key concept for extraction of $g_A(E)$ in amorphous oxide TFTs by using multi-frequency C-V technique is briefly reported [15]. Based on this technique, the comparison between a-IGZO and a-IHZO TFTs in perspective of the effective $g_A(E)$ is demonstrated for the first time. The DC performance and the negative bias stress-induced instability of a-IHZO TFT is compared with that of a-IGZO TFT.

2. Experiments

A schematic cross-section of integrated amorphous oxide TFTs with the most commonly used staggered bottom gate structure for AMLCDs is shown in Fig. 1. The procedure of a-IGZO/ a-IHZO TFT fabrication is as follows:

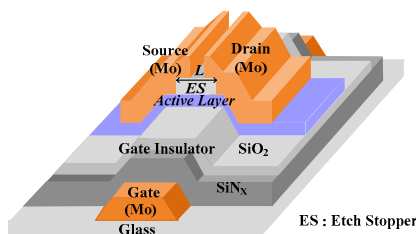


Fig. 1. Schematic cross-sectional view of the fabricated a-IGZO and/or a-IHZO TFTs which has the inverted staggered bottom gate structure.

^a electronic mail:drlife@kookmin.ac.kr

On a glass substrate, the first sputtered deposition at room temperature (RT) and patterning of molybdenum (Mo) gate are followed by plasma-enhanced chemical vapor deposition (PECVD) of gate dielectric SiN_x and SiO_2 at 370°C (T_{GI} : the equivalent oxide thickness (EOT) of $\text{SiN}_x/\text{SiO}_2$ gate insulator; $C_{ox} = \epsilon_{ox}/T_{GI}$: gate capacitance per unit area). The a-IGZO and a-IHZO active layers are then sputtered by the DC sputtering at RT in a mixed atmosphere of Ar/O₂ (35:21 at sccm) and wet-etched with diluted HF (T_{Active} : the thickness of a-IGZO and a-IHZO active layers). Etch stopper SiO_x layer is deposited by PECVD at 150 °C and patterned by wet-etching. For the formation of source/drain (S/D) electrodes, Mo is sputtered at RT and then patterned by dry-etching. A passivated layer of SiO_x and SiN_x (thickness of SiO_x and SiN_x is 100 nm, respectively) was deposited on the TFTs. Finally, the fabricated a-IGZO and a-IHZO TFTs were annealed at 300 °C and 250 °C for 1 hr in air ambient, respectively. The geometrical parameters are as follows: $T_{GI}=400/50$ nm ($\text{SiN}_x/\text{SiO}_2$)=273 nm (EOT), $W=400$ μm, $L=100$ μm, L_{ov} (gate-to-S/D overlap length)=10 μm, and $T_{Active}=50$ nm, respectively. The transfer characteristics and bias stress-induced instability of the TFTs were measured using an Agilent 4156 C semiconductor parameter analyzer.

3. DOS Extraction Technique

The extraction of the effective $g_A(E)$ in TFT is started from obtaining $C-V$ responses between the gate and S/D electrodes (the bias voltage is represented by V_{GS}) over a wide range of the small signal frequency, by using an LCR meter (HP 4284A). The measurement setup is illustrated in Fig. 2(a). As shown in Fig. 2(b), measured $C-V$ curves are very sensitive to the frequency (f) over the frequency range from $f=2$ kHz to 1 MHz. This observation is attributed to the f -dependence of capture-emission events through interface and/or bulk traps as well as parasitic S/D resistance (R_S) (*i.e.*, the supplying speed of the charging current through S/D electrodes).

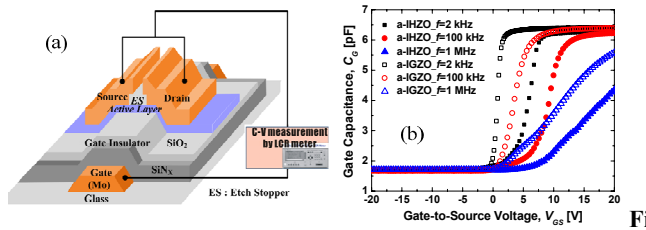


Fig. 2. (a) The schematic view of multi-frequency $C-V$ measurement setup for extracting $g_A(E)$ in active thin film. (b) The frequency-dependent $C-V$ characteristics measured by LCR meter (HP 4284A)

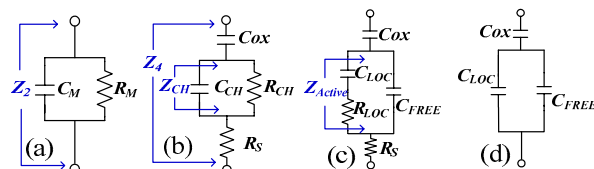


Fig. 3. (a) The 2-element capacitance model for parallel mode measurement of LCR meter, (b) the 4-element capacitance model for de-embedding of C_{ox} and R_S , (c) the physics-based capacitance model with C_{ox} , C_{LOC} , R_{LOC} , C_{FREE} , and R_S , (d) equivalent model for f -independent C_G with C_{ox} , C_{LOC} , and C_{FREE} .

Starting from the 2-element model for the measured $C-V$ data of the LCR meter (Z_2 in Fig. 3(a)), we finally obtain a frequency-independent (dispersion-free) capacitive model (Fig. 3(d)) for accurate extraction of the $g_A(E)$ in active film. In order to correlate the subgap $g_A(E)$ with the f -dependent response of capacitive components due to the modulated localized charges trapped in subgap states (Q_{LOC}), we modified the 4-element model (Z_4 in Fig. 3(b)) with the gate insulator capacitance C_{ox} , effective channel capacitance/resistance C_{CH}/R_{CH} , and R_S) into the physics-based model (Z_{Active} in Fig. 3(c)) with C_{LOC} due to V_{GS} -responsive Q_{LOC} , equivalent resistance R_{LOC} reflecting the retardation of V_{GS} -responsive Q_{LOC} , and C_{FREE} due to V_{GS} -responsive free electron charge (Q_{FREE}) in the conduction band.

In the first step, measured capacitance and resistance C_M and R_M in the 2-element model (Fig. 3(a)) are obtained from the parallel mode characterization of the LCR meter. Then, C_{ox} and R_S are de-embedded in the 4-element model in Fig. 3(b) assuming a negligible leakage current through the gate insulator due to a thick T_{GI} and frequency-independent R_S for the S/D spreading and contact resistances. In other words, the f -dependence of Z_4 is originated only from C_{CH} and C_{ox} . The impedance Z_2 in the 2-element model and Z_4 in the 4-element model are obtained to be

$$Z_2 = \frac{R_M}{1 + (\omega C_M R_M)^2} - \frac{j\omega C_M R_M^2}{1 + (\omega C_M R_M)^2}, \quad (1)$$

$$Z_4 = R_S + \frac{R_{CH}}{1 + (\omega C_{CH} R_{CH})^2} - j\left(\frac{\omega C_{CH} R_{CH}^2}{1 + (\omega C_{CH} R_{CH})^2} + \frac{1}{\omega C_{ox}}\right). \quad (2)$$

By using $Z_2 = Z_4$, we obtain R_{CH} and C_{CH} from

$$R_{CH} = \sqrt{\frac{C_M(1+D_M^2)-C_{ox}}{\omega^2 C_{CH}^2 C_{ox} - \omega^2 C_{CH} C_M(1+D_M^2)(C_{CH}+C_{ox})}}; D_M = \frac{1}{\omega C_M R_M} \quad (3)$$

$$C_{CH} = \frac{bC_{ox}^2 - b^2 C_{ox}}{\{(ab\omega)^2 + 1\} C_{ox}^2 - 2bC_{ox} + b^2}; \quad (4)$$

$$a = \frac{R_M}{\omega C_M(1+D_M^2)} - R_S, b = C_M(1+D_M^2)$$

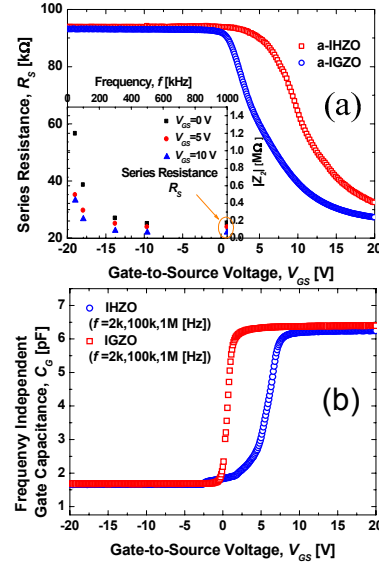


Fig. 4. (a) The extracted V_{GS} -dependent R_S obtained from the saturated magnitude of Z_2 at high frequency in the 2-element model under a fixed V_{GS} as shown in the inset. (b) The f -independent C_G for multi-frequency combinations of three frequencies extracted by using the proposed procedure.

Because the charge current is supplied through the S/D regions, the frequency dependence is influenced by the supplying speed of the charging current. Therefore $C-V$ dispersion effect of amorphous oxide TFTs by R_S component must be separated. R_S is obtained from the saturated magnitude of Z_2 at high frequency because R_S component is dominant at high frequency in the 2-element model under a fixed V_{GS} as shown in the inset of Fig. 4(a). Therefore, the V_{GS} -dependent R_S in Fig. 4(a) can be acquired, which is within the consistent range of literature (R_S extraction by using transmission line model (TLM)) [16]. The R_S of a-IHZO TFT larger than that of a-IGZO TFT is clearly observed. Here, it should be fully emphasized that there is a difference in the bias condition during the extraction of R_S in the TLM and our model ($V_S=0$ V and low V_D in the TLM while $V_S=V_D=0$ V in our model). The bias condition of $V_S=V_D=0$ V is more adequate for extracting R_S than that in the TLM for two reasons. One is that the bias condition of $V_S=V_D=0$ V agrees with the $C-V$ measurement condition. In our model, since the DOS is extracted from the frequency-dependent $C-V$ characteristics through the transformation of the equivalent model of amorphous oxide TFTs, we extracted R_S on the same condition with the $C-V$ measurement. The other is that conventional TLM is unable to reflect the R_S -induced frequency dependence of $C-V$ characteristics. Consequently, the V_{GS} - and f -dependent R_{CH} and C_{CH} can be calculated by Eqs. (3) and (4).

As the second step, the 4-element model is transformed into the *physics-based model* in Fig. 3(c). The impedance Z_{CH} composed of C_{CH} and R_{CH} in the active thin film is given by

$$Z_{CH} = \frac{R_{CH}}{1 + (\omega C_{CH} R_{CH})^2} - \frac{j\omega C_{CH} R_{CH}^2}{1 + (\omega C_{CH} R_{CH})^2}. \quad (5)$$

While the impedance Z_{Active} composed of the C_{LOC} , R_{LOC} , and C_{FREE} in the physics-based model shown in Fig. 3(c) is described as

$$Z_{Active} = \frac{C_{LOC}^2 R_{LOC}}{\omega^2 C_{LOC}^2 C_{FREE} R_{LOC}^2 + (C_{LOC} + C_{FREE})^2}, \quad (6)$$

$$-j \frac{\omega^2 C_{LOC}^2 C_{FREE} R_{LOC}^2 + (C_{LOC} + C_{FREE})}{\omega^3 C_{LOC}^2 C_{FREE} R_{LOC}^2 + \omega(C_{LOC} + C_{FREE})^2}$$

where we assume that R_{LOC} and C_{LOC} are independent of f because the product of C_{LOC} and R_{LOC} determines the frequency behavior of Q_{LOC} . By using $Z_{CH}=Z_{Active}$, we obtain

$$R_{LOC} = \sqrt{\frac{\omega^2 C_{CH} R_{CH}^2 (C_{LOC} + C_{FREE})(C_{LOC} + C_{FREE} - C_{CH}) - (C_{LOC} + C_{FREE})}{\omega^2 C_{LOC}^2 C_{FREE} [1 + \omega^2 C_{CH} R_{CH}^2 (C_{CH} - C_{FREE})]}}. \quad (7)$$

Then, by using $R_{LOC}(\omega_1)=R_{LOC}(\omega_2)=R_{LOC}(\omega_3)$ for three different frequency combinations (multi-frequency $C-V$ characteristics), all of C_{LOC} , C_{FREE} , and R_{LOC} satisfying the f -independent R_{LOC} are derived from (7). As a result of the extraction procedure with multi-frequency $C-V$ data, the f -independent gate capacitance C_G (Fig. 3(d)) with physical parameters including C_{ox} , C_{LOC} , and C_{FREE} is finally obtained as shown in Fig. 4(b). It is worthy of noting that initially measured f -dependent $C-V$ curve (Fig. 2(b)) is transformed into the f -independent one (Fig. 4(b)) based on the proposed procedure. Here, the initially assumed $C_{ox}=\epsilon_{ox}/T_{GI}$ is confirmed and if necessary, corrected by the saturated maximum value of C_G in Fig. 4(b), which is followed by iterating the procedure in (2)~(7).

Considering that C_{LOC} reflects the V_{GS} -dependent Q_{LOC} , the effective $g_A(E)$ can be extracted from

$$C_{LOC} = \frac{[C_{LOC}(V_{GS1}) - C_{LOC}(V_{GS2})]}{W \times L \times T_{Active}} \quad [F \cdot cm^{-3}] \quad (8)$$

$$g_A(E) = \frac{C_{LOC}}{q^2} \quad [eV^{-1} \cdot cm^{-3}]. \quad (9)$$

In order to obtain the nonlinear relation between V_{GS} and the energy E , we apply the Gauss' law to the interface of active thin film/gate insulator and obtain

$$V_{GS} = V_{FB} + \phi_s + \frac{Q_{LOC} + Q_{FREE}}{C_{ox}}, \quad (10)$$

$$1 = \frac{\partial \phi_s}{\partial V_{GS}} + \frac{1}{C_{ox}} \times \frac{\partial (Q_{LOC} + Q_{FREE})}{\partial V_{GS}} = \frac{\partial \phi_s}{\partial V_{GS}} + \frac{C_G}{C_{ox}}, \quad (11)$$

where ϕ_s is the surface potential. Finally, the effective $g_A(E)$ is extracted from the f -independent C_G in Fig. 4(b), (8) and (9). Here, the nonlinear relation between ϕ_s (or E) and V_{GS} can be taken into account by combining the f -independent C_G - V_{GS} curve shown in Fig. 4(b) by integrating (11) over V_{GS} as

$$\phi_s = \int_{V_{FB}}^{V_{GS}} \left(1 - \frac{C_G}{C_{ox}} \right) dV_{GS}. \quad (12)$$

4. Results and Discussions

The measured transfer (I_{DS} - V_{GS}) characteristic and field effect mobility (μ_{FE}) of a-IHZO/a-IGZO TFT are shown in Fig. 5. The extracted DC parameters are summarized in Table I. If excluding the difference of threshold voltage (V_T), The DC performance of a-IHZO TFT is comparable to that of a-IGZO TFT, in spite of larger R_S (Fig. 4(a)).

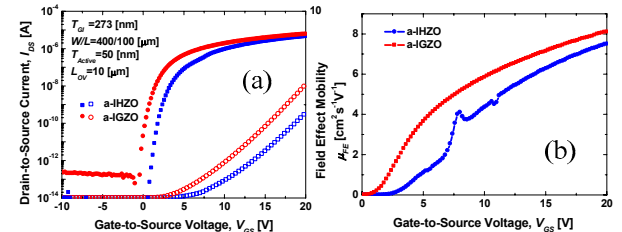


Fig. 5. The measured (a) transfer characteristic and (b) field effect mobility μ_{FE} of a-IHZO and a-IGZO TFT.

Table I. The extracted DC parameters

Parameter	a-IHZO TFT	a-IGZO TFT
Turn-on voltage V_{ON} [V]	1.23	-0.29
Threshold voltage V_T [V]	5.12	2.8
Subthreshold swing SS [V/dec]	0.575	0.521
I_{ON} at $V_{GS}=V_{DS}=20$ V [μ A]	27.54	45.01
Field effect mobility μ_{FE} [cm^2/Vs] at $V_{GS}=20$ V and $V_{DS}=1.1$ V	7.5	8.1

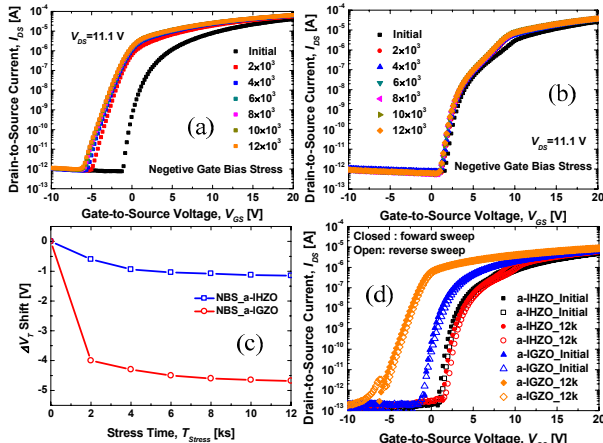


Fig. 6. The NBS time-evolution of I_{DS} - V_{GS} characteristics of (a) a-IGZO and (b) a-IHZO TFTs, (c) the measured NBS-induced ΔV_T , and (d) hysteresis characteristics of a-IGZO and a-IHZO TFTs before and after NBS

Additionally, the negative bias stress (NBS) time-evolution of I_{DS} - V_{GS} characteristics of a-IGZO and a-IHZO TFTs are shown in Fig. 6(a) and 6(b). The negative bias condition is $V_{GS} = -20$ V/ $V_{DS} = 10$ V, which is the switch OFF condition during most of each cycle time in real display pixel operation. The NBS-induced V_T shift (ΔV_T) of a-IGZO TFT is larger than that of a-IHZO TFT as shown in Fig. 6(c). And Fig. 6(d) shows the hysteresis characteristics of a-IGZO and a-IHZO TFTs before and after NBS for 1.2×10^{14} s. The NBS-induced increase of interface and/or in-film trap, border trap in gate dielectric is insignificant, because there is no increase of hysteresis during NBS. Therefore, the NBS-induced ΔV_T can be attributed to the electron detrapping (or hole trapping).

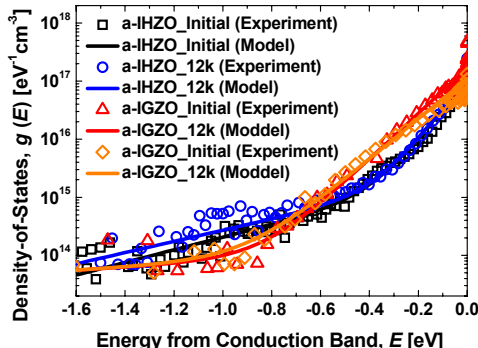


Fig. 7. The NBS time-evolution of $g_A(E)$ in a-IGZO and/or a-IHZO TFT, which is extracted by using multi-frequency C-V technique.

The NBS time-evolution of $g_A(E)$ extracted by using multi-frequency C-V technique is shown in Fig. 7, which exhibits the superposition of exponential tail states and exponential deep states as seen in (13). The model parameters for extracted $g_A(E)$ are summarized in Table II.

$$g_A(E) = N_{TA} \times \exp\left(-\frac{(E_C - E)}{KT_{TA}}\right) + N_{DA} \times \exp\left(-\frac{(E_C - E)}{KT_{DA}}\right) \quad (13)$$

Although the R_S of a-IHZO TFT is larger than that of a-IGZO TFT (Fig. 4(a)), the DC performance of a-IHZO TFT is comparable to that of a-IGZO TFT, which is most probably due to lower tail states of $g_A(E)$ (Fig. 7). On the other hand, the NBS-induced change of $g_A(E)$ is observed to be insignificant. It is consistent with Fig. 7, because the dynamic trapping via $g_A(E)$ is related to the hysteresis phenomenon [17]. Thus, the $g_A(E)$ is not likely to greatly influence on the NBS-induced ΔV_T . Compared with a-IGZO TFT, although the mechanism of superior stability in a-IHZO TFT is not clear because the donor-like DOS $g_D(E)$ near valence band edge is still unknown, the difference of $g_D(E)$ between a-IGZO and a-IHZO TFTs may play a role of the NBS-induced instability. The $g_D(E)$ is likely to act as the electron detrapping (or hole trapping) center in active thin film. Further study is required.

Table II. Model parameters of extracted $g_A(E)$

Parameter	a-IHZO TFT		a-IGZO TFT	
	Initial	12k	Initial	12k
N_{TA} [eV ⁻¹ cm ⁻³]	1.1×10^{17}	1.1×10^{17}	1.7×10^{17}	1.1×10^{17}
kT_{TA} [meV]	80	80	110	125
N_{DA} [eV ⁻¹ cm ⁻³]	2.5×10^{15}	2.5×10^{15}	1.5×10^{14}	1.5×10^{14}
kT_{DA} [eV]	0.4	0.45	1.6	1.6

5. Acknowledgements

This work was supported by the Korea Science and Engineering Foundation (KOSEF) grant funded by the Korea government (MEST) (No. 2009-0080344).

6. References

- [1] J. Y. Kwon *et al.*, IEEE Electron Device Lett., vol. 29, p. 1309, 2008.
- [2] Y. Ohta *et al.*, Proc. Int. Display Workshop, 2009, p. 1685.
- [3] J. Sakata *et al.*, Proc. Int. Display Workshop, 2009, p. 689.
- [4] J.-H. Lee *et al.*, SID 08 Dig., 2008, p. 625.
- [5] J.-M. Lee *et al.*, Appl. Phys. Lett., vol. 94, p. 222112, 2009.
- [6] A. Suresh and J. F. Muth, Appl. Phys. Lett., vol. 92, p. 033502, 2009.
- [7] C.-J. Kim *et al.*, Appl. Phys. Lett., vol. 95, p. 252103, 2009.
- [8] W. H. Jeong *et al.*, Proc. Int. Display Workshop, 2009, p. 1795.
- [9] S. Lee *et al.*, Appl. Phys. Lett., vol. 95, p. 132101, 2009.
- [10] H.-H. Hsieh *et al.*, Appl. Phys. Lett., vol. 92, p. 133503, 2008.
- [11] M. Kimura *et al.*, Appl. Phys. Lett., vol. 92, p. 133512, 2008.
- [12] K. Jeon *et al.*, Appl. Phys. Lett., vol. 93, p. 182102, 2008.
- [13] J.-H. Park *et al.*, IEEE Electron Device Lett., vol. 29, p. 1292, 2008.
- [14] C. Chen *et al.*, IEEE Transactions on Electron Dev., vol. 56, p. 1177, 2009.
- [15] S. Lee *et al.*, IEEE Electron Device Lett., vol. 31, p. 231, 2010.
- [16] J. Park *et al.*, IEEE Electron Device Lett., vol. 29, p. 879, 2008.
- [17] J.-H. Lee *et al.*, J. Non-Cryst. Solids, vol. 352, p. 1719, 2006